



Available online at
ScienceDirect
www.sciencedirect.com

Elsevier Masson France
EM|consulte
www.em-consulte.com/en



Original article

Non-destructive imaging of ancient marquetry using active thermography and photothermal coherence tomography



Pantea Tavakolian^{a,*}, Elnaz B. Shokouhi^a, Stefano Sfarra^b, Gianfranco Gargiulo^c, Andreas Mandelis^{a,*}

^a Center for Advanced Diffusion-Wave and Photoacoustic Technologies (CADIPT), Department of Mechanical and Industrial Engineering, University of Toronto, Toronto, Ontario M5S3G8, Canada

^b Department of Industrial and Information Engineering and Economics (DIIE), University of L'Aquila, Monteluco di Roio – L'Aquila (AQ) I-67100, Italy

^c Individual company of restoration (Gianfranco Gargiulo), Via Tiberio 7b, Capri (NA) I-80073, Italy

ARTICLE INFO

Article history:

Received 19 February 2020

Accepted 13 May 2020

Available online 24 June 2020

Keywords:

Active thermography
Lock-in thermography
Enhanced truncated-correlation
photothermal coherence tomography
Art conservation
Non-destructive evaluation
Marquetry defectoscopy

ABSTRACT

Active thermography has proven successful for non-destructive evaluation of art objects. The aim of this work was to detect the defects of a genuine ancient marquetry sample with both enhanced truncated correlation photothermal coherence tomography (eTC-PCT) and the well-known lock-in thermography (LIT) and compare the two modalities. Quantitative analysis of eTC-PCT images for depth measurements was also performed. Both methods revealed worn-off and glue starved areas, cracks and detachments in the sample, all of which are common defects of these types of art objects. In comparison, the eTC-PCT method was proven to be able to provide 3D images of the interrogated sample and more information about deep sub-surface defects with better contrast than LIT. Moreover, the eTC-PCT results of the marquetry sample containing natural defects were analyzed to determine the location of defects, a task that is not possible with LIT. The experiments showed that both methods are safe for non-destructive evaluation of art samples with temperature rise of less than 0.8 °C using eTC-PCT, and less than 1.5 °C using the LIT method.

© 2020 Elsevier Masson SAS. All rights reserved.

1. Introduction

Inspection methods of cultural heritage objects have held prominence, especially those capable of obtaining information about their physical condition for restoration and preservation purposes. Among the most notable inspection methods, non-destructive evaluation (NDE) has been extensively used to investigate the state of valuable and delicate cultural pieces that would otherwise be harmed or destroyed if destructive testing methods were employed. Between the 12th and the 20th century, most museums and collectors used visual assessment or identification checklists in order to perform non-destructive evaluation of objects [1]. Currently, various imaging modalities such as X-rays [2], ultrasound [3], THz-time domain spectroscopy [4], thermography [5], and Raman spectroscopy [6] are being utilized for non-destructive analysis of such objects. Among the most relevant NDE methods, active thermography holds an important place and

various studies have proved its feasibility in examination of cultural heritage objects, art works [7–10], and archeological artifacts composed of various structures and materials [11]. Complementary to this method, researchers have also investigated the state of conservation of such objects at various excitation wavelengths [12,13].

Lock-in thermography (LIT), a popular active thermography technique is designed to produce depth-integrated two-dimensional (2-D) amplitude and phase images of temperature oscillations in a sample ("thermal waves") in which light absorbing features within the thermal diffusion length are superposed. Here, a sample is excited at a certain frequency and the demodulated output signal is recorded. By changing the modulation frequency, the contrast between various surface and subsurface features can be adjusted to produce high signal-to-noise ratio (SNR) thermal wave images [14].

Similar to LIT, another modality known as enhanced-truncated-correlation photothermal coherence tomography (eTC-PCT) [15] incorporates matched-filter thermography, a time-evolving temporal filter, and cross-correlation signal processing and analysis in order to resolve the depth-integrated nature of other dynamic thermography techniques such as LIT, TC-PCT [16], and its enhanced

* Corresponding authors.

E-mail addresses: ptavakolian@gmail.com (P. Tavakolian), mandelis@mie.utoronto.ca (A. Mandelis).

version, eTC-PCT [15] are dynamic thermal imaging modalities that provide depth-resolved three-dimensional (3-D) amplitude and phase images of objects. Despite eTC-PCT's recent development, it has already proven its diagnostic capability in the field of inlay analysis and defectoscopy [9]. Nevertheless, minimal research effort has been focused on an objective comparison of the capabilities of eTC-PCT with other dynamic thermography techniques toward the detection of natural defects in historical artifacts, unlike LIT which has been used for decades in the field of defectoscopy. Therefore, in this paper, the eTC-PCT method was investigated for the NDE of ancient art objects and compared with LIT. An ancient marquetry sample with natural defects was tested, the decorative layer of which was composed of various materials, among which some nacre's tesserae. A preliminary visual inspection validation was conducted by a professional restorer.

Additionally, the data captured from artificially fabricated defects within an inlay object that was investigated in a previous study [9] were analyzed in order to acquire depth information and compare with the known actual depth. Then, a genuine art piece was analyzed to provide more depth information regarding the defects within that sample.

2. Methods

2.1. Experimental setup

The eTC-PCT and LIT experimental setup, Fig. 1, includes a mid-infrared camera (A6700sc, FLIR, USA, 3–5 μm spectral response), a function generator (Keysight 33500B, USA), a high-speed data acquisition module for recording the excitation signal (NI PCI-6281), and an 808-nm diode laser (Jenoptic JOLD-120-QPXF-2P) controlled by a laser driver (PCO-6131, Directed Energy, Colorado,

USA). The beam homogenizer is built with a collimator (F22SMA-B, Thorlabs Inc., New Jersey, USA) and a diffuser (ED1-C20, Thorlabs Inc., New Jersey, USA).

2.2. Enhanced-truncated correlation photothermal coherence tomography (eTC-PCT)

Briefly, the eTC-PCT reconstruction algorithm provides 2-D image slices of the sample and three dimensional tomographic views of the sample. The reconstruction algorithm is explained in detail elsewhere [14]. For this study, the experimental excitation pulsed chirp radar parameters were: starting frequency 0.2 Hz, ending frequency 0.4 Hz, chirp period 17 s, excitation pulsewidth 70 ms, and 60 W laser peak power. A reference waveform with a sweep-delay step of 20 ms was used to generate a stack of 55 2-D images. The imaged area was 8 cm \times 6.4 cm on the sample surface, and the camera was operated at its full window of 640 \times 512 pixels. Averaging of 4 pixels resulted in image size of 160 \times 128 pixels, and lateral resolution of 0.5 mm. The camera frame rate was 104 Hz. For this set-up, laser beam diameter was 11.5 cm, and the 70 ms excitation pulsewidth delivered energy of $\sim 40 \text{ mJ cm}^{-2}$ per pulse to the sample.

2.3. Lock-in thermography

Unlike eTC-PCT, the LIT signal processing algorithm is designed to produce a 2-D amplitude and a 2-D phase image. Hence, LIT only performs at a fixed modulation frequency in which the sample surface temperature profiles are captured by an IR camera. The LIT reconstruction algorithm used in this work is thoroughly described elsewhere [17]. It is important to note that while the LIT system setup is similar to that of eTC-PCT, however, instead of

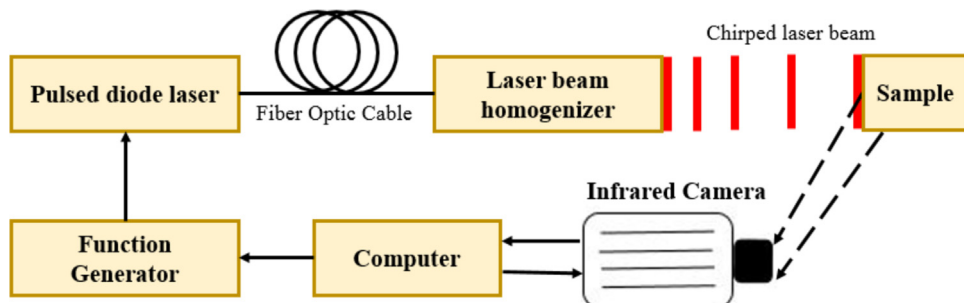


Fig. 1. TC-PCT system setup.

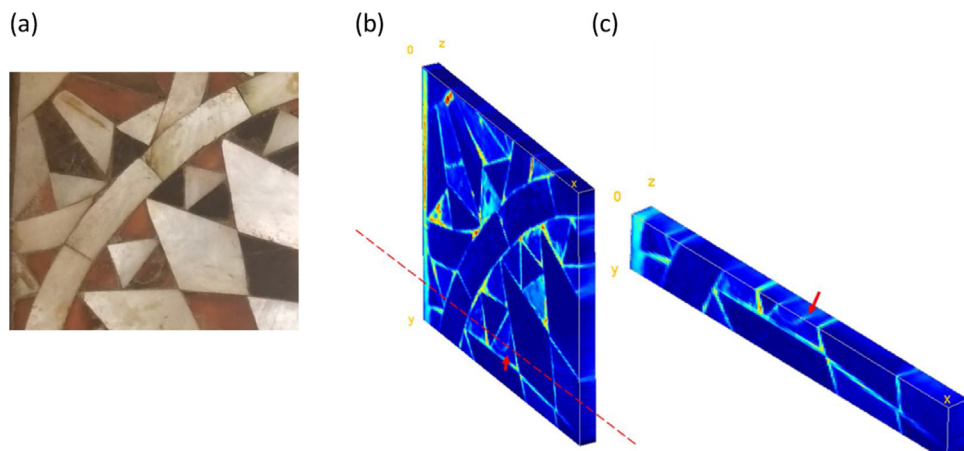


Fig. 2. 3D eTC-PCT imaging. (a) Top down picture of the imaged area (location 1, Loc 1) on the surface of the marquetry sample. (b) 3D eTC-PCT of the imaged area. (c) cut portion of the volumetric image to visualize the depth and subsurface shape of crack.

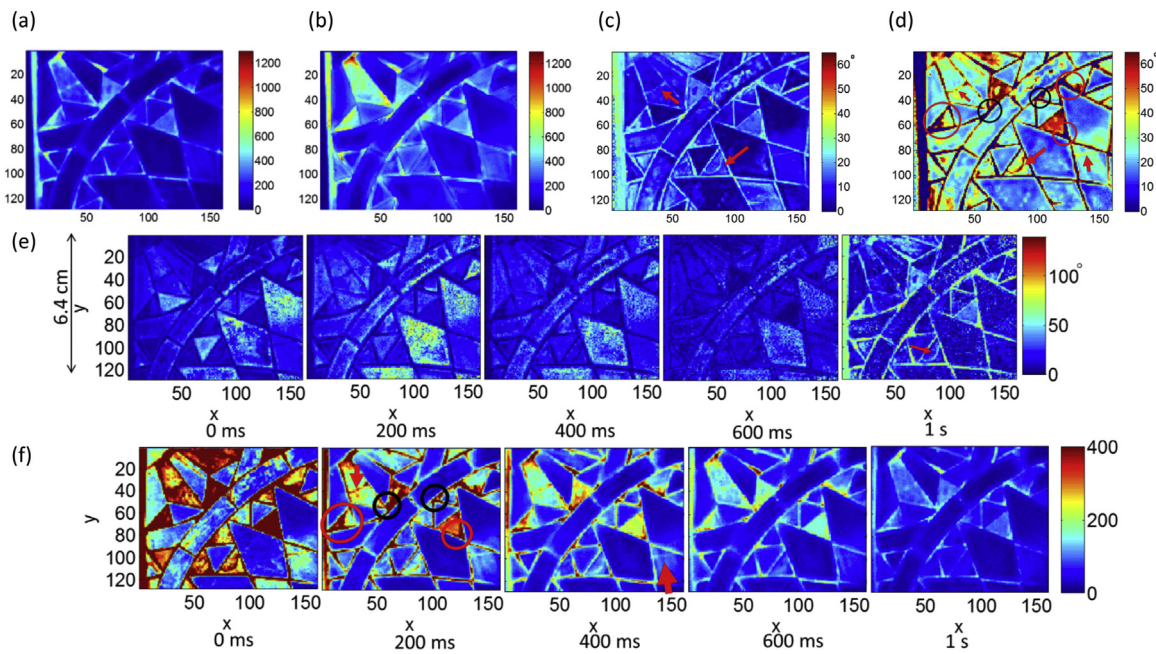


Fig. 3. LIT and eTC-PCT images of location 1 (Loc 1) on the marquetry sample. LIT amplitude images of Loc1 at (a) 0.2 Hz and (b) 0.4 Hz. LIT phase images of Loc1 at (c) 0.2 Hz and (d) 0.4 Hz. Planar phase (e) and amplitude (f) eTC-PCT image slices at various depths starting from the surface at $t=0$ ms and proceeding to deeper layers inside the sample. Here, cracks are shown with red arrows, and worn-off areas and glue-starved connections between top tesserae are indicated inside red and black circular areas, respectively.

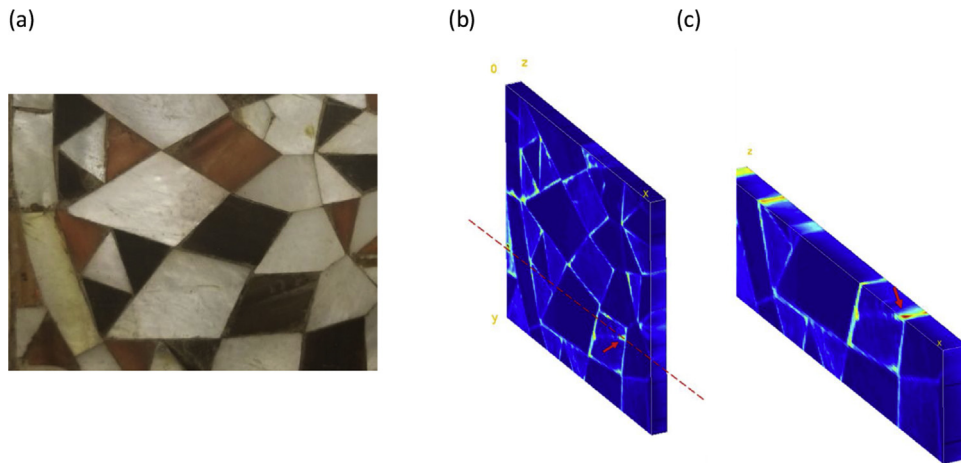


Fig. 4. 3D eTC-PCT imaging. (a) Top down picture of the imaged area (location 2, Loc 2) on the surface of the marquetry sample. (b) 3D eTC-PCT of the imaged area. (c) cut portion of the volumetric image to visualize the depth and subsurface shape of crack.

using pulsed chirped radar parameters, fixed-period square-wave modulation is used to excite the sample. For comparison of eTC-PCT with LIT, three square-wave laser waveforms were used at 0.2 Hz, 0.3 Hz, and 0.4 Hz with experimental duration of 17 s. Reconstruction of LIT images with the 0.2 Hz and 0.4 Hz square wave exhibited the best results for studying the experimental parameter effects such as modulation frequency. In addition, the frequencies chosen for analysis were at the lower and the upper ends of the eTC-PCT excitation signal sweep range which allows for reasonable comparison of the two methods. The imaged area was the same as that of the eTC-PCT experiment, and the camera was operated at its full window of 640×512 pixels. The camera frame rate was 104 Hz. For this set-up, laser beam diameter was 11.5 cm, and the per pulse excitation fluence incident on the sample was $\sim 195 \text{ mJ cm}^{-2}$.

3. Results and discussion

Photothermal images of two areas on the ancient marquetry samples were obtained. Both LIT and eTC-PCT imaging methods were used to image these areas and two different locations on the art sample were examined. A visible photograph of the first location on the sample and the 3D eTC-PCT image of this location is shown in Fig. 2 (a and b). The LIT amplitude and phase images of the first location (Loc1) obtained at 0.2-Hz and 0.4-Hz square-wave are displayed in

Fig. 3(a-d). A sequence of 2-D eTC-PCT amplitude and phase images of the same location are presented in Fig. 3(e and f).

A visible photograph of the second location on the sample and the 3D eTC-PCT image of this location is shown in Fig. 4 (a-b). In a similar order, for the second location (Loc2), the same sequence

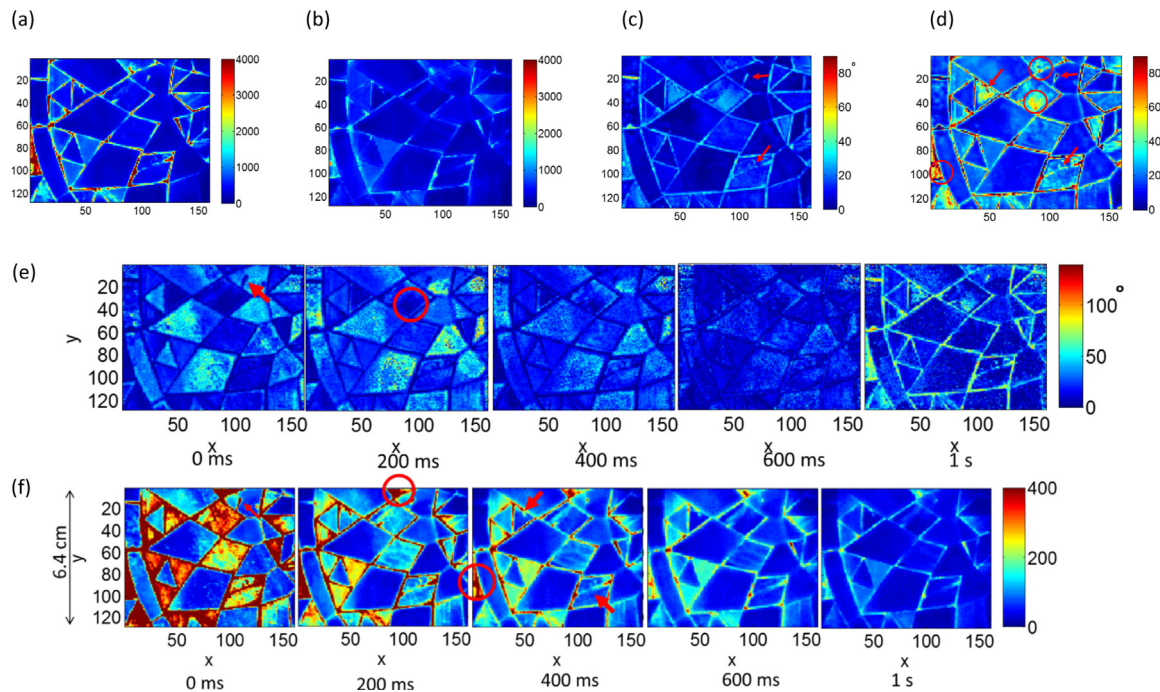


Fig. 5. LIT and eTC-PCT of location 2 (Loc2) on the marquetry sample. LIT amplitude images of this location at (a) 0.2 Hz and (b) 0.4 Hz. LIT phase images of Loc2 at (c) 0.2 Hz and (d) 0.4 Hz. Planar phase (e) and amplitude (g) eTC-PCT image slices at various depths starting from the surface at $t = 0$ ms and proceeding to deeper layers inside the sample. Here, cracks are shown with red arrows, and worn-off areas and glue-starved connections between top tesserae are indicated inside red and black circular areas, respectively.

displays the amplitude and phase images of LIT at 0.2 Hz and 0.4 Hz in Fig. 5(a-d), and eTC-PCT phase and amplitude images in Fig. 5(e and f). While both amplitude and phase images are shown in this paper, only phase images are used for discussion as they carry more information about the sample and are emissivity normalized. To mark the location of various defects on the LIT and eTC-PCT phase images, cracks are shown with red arrows, while worn-off areas and glue-starved connections between top tesserae are indicated inside red and black circular areas, respectively.

The visual inspection of amplitude and phase images of LIT and eTC-PCT shows that both methods were capable of detecting the sharp borders between the individual tesserae, and surface inhomogeneities and height differences between adjacent tesserae. In LIT, high frequencies (here 0.4 Hz) are better suited for detection of inhomogeneities that are located close to the surface as the thermal diffusion length is inversely proportional to the square root of frequency. While both frequencies can show the existing cracks, the lower frequency (0.2 Hz) shows more details of the depth and extent of the cracks on the ancient marquetry as can be seen in Fig. 3(c). Here, again, the phase image taken at 0.2 Hz provides a better indication of deeper features such as worn-off and glue-starved areas that might potentially wear off in the future.

In Loc2, while both LIT phase images at 0.2 and 0.4 Hz (Fig. 5(c and d)) show features such as cracks on the individual tesserae of the art sample and areas prone to wearing-off, the phase image taken at 0.4 Hz only provides information about the surface features of the sample. With the information provided by the LIT phase images at 0.4 Hz, it is important to note that some of these features and inhomogeneities can also be seen visually on the art sample with the naked eye. The phase image at 0.2 Hz provides details about areas that certainly have cracks or worn off areas, while the phase image taken at 0.4 Hz only shows few of these defects in the art sample.

In eTC-PCT, all the defects including crack and worn-off or glue starved areas are detected with a higher contrast than that

of LIT and with the benefit of combining the advantages of both high (0.4 Hz) and low (0.2 Hz) LIT frequencies. Therefore, all these defects including cracks, worn-off areas, and glue-starved connections can be detected in a single eTC-PCT imaging experiment and in the sequence of 2-D eTC-PCT images, information about surface and deep defects, including the subsurface shape of the defect, can also be distinguished. The depth-integrated nature of LIT does not provide tomographic maps of internal features that are visible in phase images at 0.2 Hz and it does not allow quantification of geometric parameters such as depth and shape of subsurface features.

In 3-D eTC-PCT image of Loc1 (Fig. 2(b)), a section of the tomographic image has been sliced to investigate the internal features of the a crack that is shown by the red arrow. The crack (Fig. 2(c)) seems to be a superficial crack as its in-depth contrast deteriorates quickly. The 3-D eTC-PCT image of Loc2 is cut at the dashed line (Fig. 4(b)) to visualize the depth-resolved information of another crack that is also shown in the image by the red arrow. As can be seen in (Fig. 4(c)), the crack starts at the surface of the marquetry and maintains its high contrast midway through the sample. The contrast then deteriorates indicating that at depths beyond that point, there is no sign of crack. Hence, the 3-D image reconstruction property of eTC-PCT enables the understanding of the severity and depth of cracks as well as the quality of the connections between tesserae of different materials on the top layer. This aspect not only detects cracks which can be seen visually from the tomographic images, but also provides qualitative defect depths and shapes. To further explore this feature, a measurement was made of the defect depths on an inlay sample with known artificial defects reported earlier using eTC-PCT [9].

Three of the defects of the inlay were selected and are presented in Fig. 6(a-c): one with a full through hole within a middle layer of the sample beneath the top layer with a thickness of 0.7 mm, a second one with a half drilled hole within the middle layer, and a third one with a through hole filled with stucco and charcoal. The imaged area on the front or rear surface of the marquetry sample,

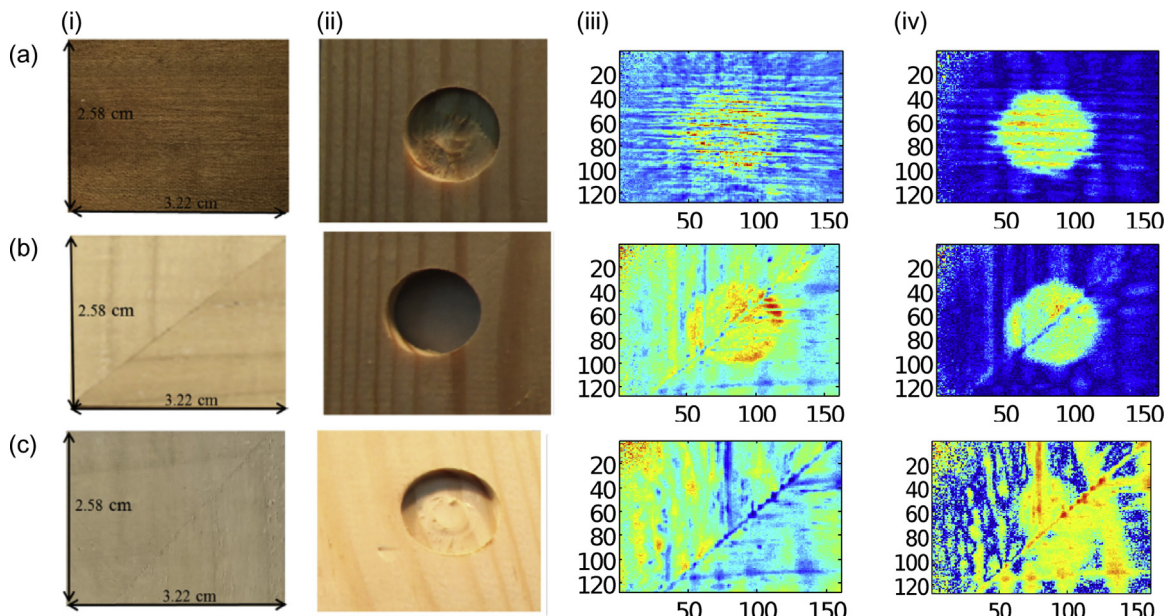


Fig. 6. Depth measurement of defects using eTC-PCT. (i) Three photographs on the first column display the imaged area on the rear side of the defects (through hole in the middle layer (a), half drilled hole in the middle layer (b), and through hole filled with stucco plus charcoal (c)) (ii) Three photographs on the second column display the hidden middle layer defect underneath the imaged area. (iii) Three figures on the third column display the defects on the highest contrast eTC-PCT slice. (iv) Three figures on the fourth column display the corresponding defects on the highest contrast eTC-PCT slice. The through hole highest contrast slice is at slice number 46 (a), while the half-drilled hole (b), and stucco plus charcoal (c) are showing the highest contrast at slice 43 and 10, consequently. For reconstructing eTC-PCT images of the hole and stucco plus charcoal, excitation and reference pulse width of 10 ms and 30 ms were selected, respectively.

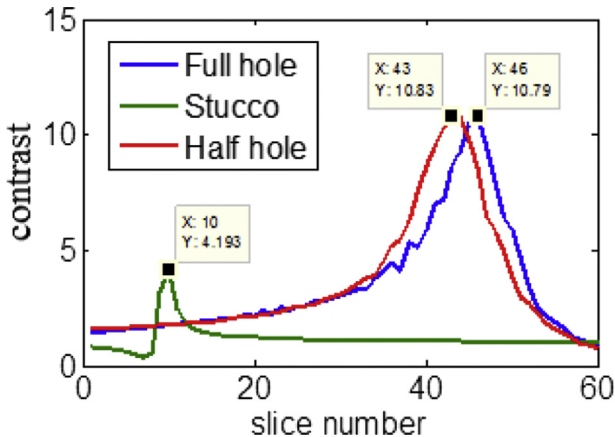


Fig. 7. The three plots display phase contrasts of the defects with substrate as a function of the slice number. Based on the time of the highest contrast image, the approximate depth of the defects can be measured. Because these defects are artificially located beneath 0.7 mm of wood, with knowledge of the thermal diffusivity of the sample the defect, the depths were measured experimentally as shown in the table, matching well with the real depth.

and the hidden middle layer underneath the imaged area are presented in columns (i), and (ii) of each figure, respectively. eTC-PCT phase images of the defects were acquired. For each eTC-PCT slice, the defect contrast was measured in relation to the substrate. The contrast was found to increase and then decrease. eTC-PCT images of the defects in slice 1 (surface image) and the slice that has the highest defect contrast are displayed in column (iii) and (iv), respectively. Then, the contrast value was plotted as a function of slice number, Fig. 7. The through hole has its highest contrast at slice number 46, while the half-drilled hole and stucco display their highest contrast at slice 43 and 10, respectively. These numbers of eTC-PCT slices are acquired from the peaks of the contrast plots shown in Fig. 7.

The time-dependent thermal diffusion length for an opaque sample (considering one dimensional thermal diffusion, which is reasonable because of the large beam diameter) is $\frac{2\sqrt{\alpha t}}{\sqrt{\pi}}$ (where α is thermal diffusivity, and t is time) [15]. Based on the peak contrast time, the approximate depth of the defects can be measured, since this slice corresponds to the location of the artificially located defect beneath 0.7 mm of wood. Knowledge of the thermal diffusivity of the sample can be used to measure defect depths experimentally using the time-dependent thermal diffusion length. The measured values are in approximate agreement with the real depth of the defects except for the stucco “defect”. The difference between the measured and real depth can be explained by considering the fact that stucco comprises a mixture of charcoal and stucco glued to the middle layer which alters the pure thermal diffusivity value of the stucco itself. For reconstructing eTC-PCT images of the hole and stucco, excitation and reference pulse widths of 10 ms and 30 ms, respectively, were selected. The longer pulse width of the excitation signal allows enough time for the thermal signal to diffuse which means that the thermal signals from different layers are mixed in eTC-PCT slices. Therefore, the time resolved characteristics of eTC-PCT are not fully preserved.

On the ancient marquetry sample, three locations corresponding to a worn-off area on a nacre's tessera, a crack, and a loose connection (glue starved area) were selected and the phases of the thermal responses in time were considered. Then, the normalized phase values were plotted as a function of slice number, Fig. 8(a). While the phase should increase with increasing depth, here, a different pattern is seen caused by the defects. The defect contrast is plotted as a function of the slice number, Fig. 8(b). In the previous study of the custom built inlay sample [9], the maximum contrast of the defects corresponded to the real depth of the defect. Here, however, only a qualitative understanding of the defect depth can be gained because the excitation pulse-width was 70 ms, which is too long for accurate measurement of the depth, because the time-resolved aspect of eTC-PCT is not preserved. Fig. 8(b)

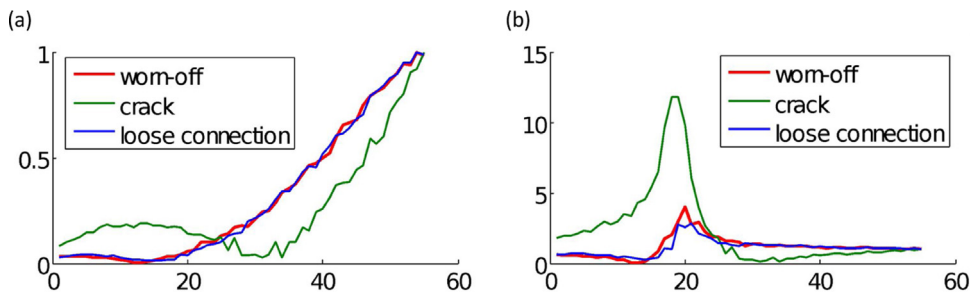


Fig. 8. Phase eTC-PCT analysis. (a) Normalized phase values of three different areas on the art sample as a function of slice number (time/depth). These three cases are worn-off area on the surface, a crack, and a loose connection between two top tesserae. (b) Contrast of the phase values as a function of the slice number.

indicates that the crack is shallower than the worn-off area and the loose connection in this example.

4. Conclusions

In this study, an ancient marquetry sample having natural defects was tested using eTC-PCT and LIT imaging. Experimental results from a mock-up were also obtained. In comparison, eTC-PCT provided a better resolution and image quality than lock-in thermography under the same experimental conditions. The reason for higher axial resolution is the time-evolving filter which truncates the cross-correlation result and enhances the SNR from a specific depth. This feature of eTC-PCT also provides a series of 2-D images which can be stacked to obtain a 3-D view of the sample. The 3D non-destructive imaging feature is an important advantage of the eTC-PCT technique, that should be welcomed by restorers designed to devise minimally invasive and low cost inspection practices of precious historical and heritage objects. Contrast peaks of eTC-PCT images can yield the approximate depth of various subsurface defects within an art object, which adds valuable information for conservation of the art sample. In the lock-in thermography and eTC-PCT experiments, the maximum temperature changes on the marquetry sample were 1.8 °C and 0.8 °C, respectively. In the future, inspection with eTC-PCT and non-destructive 3-D imaging of samples will be explored at various excitation wavelengths and will be compared with the current study in order to improve defect detection and analysis.

Acknowledgements

The authors gratefully acknowledge the Natural Sciences and Engineering Research Council (NSERC) Discovery Grants Program, the Canada Foundation for Innovation (CFI) Research Chairs Program, and the NSERC – Collaborative Research and Training Experience (CREATE) for financial support.

References

- [1] P.T.V. Gutierrez, S.C. Robinson, Determining the presence of spalted wood in Spanish marquetry woodworks of the 1500s through the 1800s, *Coatings* 7(11) (2017) 1–14.
- [2] J.J. Chen, A. Shugar, A. Jehle, X-radiography of cultural heritage materials using handheld XRF spectrometers, *X-ray Spectrom.* (2018).
- [3] R.G. Maev, R.E. Green Jr., A.M. Siddiqi, Review of advanced acoustical imaging techniques for nondestructive evaluation of art objects, *Res. Nondestruct. Eval.* 17 (2006) 191–204.
- [4] M. Picollo, K. Fukunaga, J. Labaune, Obtaining noninvasive stratigraphic details of panel paintings using terahertz time domain spectroscopy imaging system, *J. Cult. Herit.* 16(1) (2015) 73–80.
- [5] F. Mercuri, C. Cicero, N. Orazi, S. Paoloni, M. Marinelli, U. Zammit, Infrared thermography applied to the study of cultural heritage, *Int. J. Thermophys.* 36(5–6) (2015) 1189–1194.
- [6] P. Vandenabeele, B. Wehling, L. Moens, H. Edwards, M. De Reu, G. Van Hooydonk, Analysis with micro-Raman spectroscopy of natural organic binding media and varnishes used in art, *Anal. Chim. Acta* 407(1) (2000) 261–274.
- [7] J.L. Bodnar, J.L. Nicolas, J.C. Candoré, V. Detalle, Non-destructive testing by infrared thermography under random excitation and ARMA analysis, *Int. J. Thermophys.* 33 (2012).
- [8] S. Laureti, et al., Development of integrated innovative techniques for painting examination: the case studies of The Resurrection of Christ attributed to Andrea Mantegna and the Crucifixion of Viterbo attributed to Michelangelo's workshop, *J. Cult. Herit.* 40 (2019) 1–16.
- [9] P. Tavakolian, S. Sfarra, G. Gargiulo, K. Sivagurunathan, A. Mandelis, Photothermal coherence tomography for 3-D visualization and structural non-destructive imaging of a wood inlay, *Infrared Phys. & Technol.* 91 (2018) 206–213.
- [10] F. Mercuri, U. Zammit, N. Orazi, et al., Active infrared thermography applied to the investigation of art and historic artefacts, *J. Therm. Anal. Calorim.* 104 (2011) 475.
- [11] F. Scudieri, F. Mercuri, R. Volterri, Non-invasive analysis of artistic heritage and archaeological findings by time resolved IR thermography, *J. Therm. Anal. Calorim.* 66 (2001) 307–314.
- [12] J. Peeters, G. Van der Snickt, S. Sfarra, S. Legrand, C. Ibarra-Castanedo, K. Janssens, G. Steenackers, IR reflectography and active thermography on artworks: the added value of the 1.5–3 μm band, *Appl. Sci.* 8(1) (2018) 50.
- [13] S. Sfarra, P. Theodorakeas, J. Černecký, E. Pivarciová, S. Perilli, M. Kouí, Inspecting marquetry at different wavelengths: the preliminary numerical approach as aid for a wide-range of non-destructive tests, *J. Nondestruct. Eval.* 36(1) (2017) 6.
- [14] P. Tavakolian, A. Mandelis, Perspective: principles and specifications of photothermal imaging methodologies and their applications to non-invasive biomedical and non-destructive materials imaging, *Appl. Phys. Lett.* 124(16) (2018) 160903.
- [15] P. Tavakolian, K. Sivagurunathan, A. Mandelis, Enhanced truncated-correlation photothermal coherence tomography with application to deep subsurface defect imaging and 3-dimensional reconstructions, *J. Appl. Phys.* 122 (2017) 023103.
- [16] S. Kaipalvi, A. Mandelis, Truncated-correlation photothermal coherence tomography for deep subsurface analysis, *Nat. Photonics* 8(8) (2014) 635–642.
- [17] A. Melnikov, et al., Single frequency thermal wave radar: a next-generation dynamic thermography for quantitative non-destructive imaging over wide modulation frequency ranges, *Rev. Sci. Instrum.* 89(4) (2018) 44901.